

Small-scale convective turbulence constrains microbial patchiness

A. K. Christensen^{*1}, M. D. Piggott², E. van Sebille³, M. van Reeuwijk⁴, S. Pawar¹

¹Department of Life Sciences, Imperial College London, UK

²Department of Earth Science and Engineering, Imperial College London, UK

³Utrecht University, The Netherlands

⁴Department of Civil and Environmental Engineering, Imperial College London, UK

*correspondence and requests for materials should be addressed to A. K. Christensen (a.christensen17@imperial.ac.uk).

Abstract

Microbes play a primary role in aquatic ecosystems and biogeochemical cycles. Patchiness is a critical component of these activities, influencing biological productivity, nutrient cycling and dynamics across trophic levels. Incorporating spatial dynamics into microbial models is a long-standing challenge, particularly where small-scale turbulence is involved. Here, we combine a realistic simulation of turbulence with an individual-based microbial model to test the key hypothesis that the coupling of motility and turbulence drives intense microscale patchiness. We find that such patchiness is depth-structured and requires high motility: Near the fluid surface, strong convective turbulence overpowers motility, homogenising motile and non-motile microbes equally. In deeper, thermocline-like conditions, highly motile microbes are up to 1.6-fold more patch-concentrated than non-motile microbes. Our results demonstrate that the delicate balance of turbulence and motility that triggers micro-scale patchiness is not a ubiquitous consequence of motility, and that the intensity of such patchiness in real-world conditions is modest.

1 Introduction

Life on Earth is predominantly microbial¹, with microbes responsible for the majority of the metabolic activity that maintains the basic habitability of the planet^{2,3}. Aquatic microbes

19 account for over 50% of global primary productivity in our oceans and lakes⁴, and are also
20 largely responsible for the decomposition of organic matter and recycling of nutrients^{5–8}.
21 These functions are driven by complex interactions between and among microbial individuals
22 and their environment. Precisely because they comprise so many connected components,
23 accurately modelling these complex interactions and understanding how they play out across
24 spatial and temporal scales, remains a major empirical and theoretical challenge⁹.

25 Spatial heterogeneity, or “patchiness”, is a critical component of microbial communities.
26 Patchiness at large scales ($\gtrsim 0.5$ km) has been documented since at least the 1930s^{10,11}, and
27 though the traditional assumption that turbulence would homogenise microbe distributions
28 at smaller scales^{12–14} held for much longer, we increasingly understand patchiness to be
29 common across spatial scales from millimetres to 100s of kilometers^{15–18}.

30 Patchiness matters because it can have both negative and positive effects on micro-
31 bial populations, leading to wider ecosystem-level consequences. For example, microbial
32 growth rates are higher within patches formed in nutrient hotspots or dissolved organic mat-
33 ter (DOM) plumes^{19,20}. On the other hand, microbes experience increased mortality when
34 planktonic predators leverage their own motility and sensory abilities to exploit patches²¹, or
35 because of increased viral transmission rates in patch-dwelling microbes^{22,23}. Furthermore,
36 patchiness at the smallest (≤ 1 m) scales has its own particular suite of consequences, in-
37 tensifying competition for nutrients within microbe patches⁹, colonising disproportionately
38 high-growth micro-habitats²⁰ and establishing a basis for the formation of patches of other
39 organisms of higher trophic levels²⁴. The effects of patchiness on microbial populations can
40 ultimately impact the dynamics of the wider ecosystem. For example, temporal or spa-
41 tial separation of phytoplankton and zooplankton patches can increase primary productivity
42 several-fold relative to a homogeneous environment²⁵, the aggregation of diatom detritus
43 can increase bacterial species richness and abundance²⁶, and strong patchiness in competing
44 plankton species has even been proposed as an explanation for Hutchison’s long standing
45 “paradox of the plankton”^{27,28}.

46 Spatial dynamics and microbial patchiness are thus clearly critical to understanding
47 aquatic ecosystems. However, measuring and modelling their influence is difficult due to
48 the variety and complexity of flow regimes present in nature. Turbulent flows are a partic-

49 ularly thorny area of research; naturally-occurring turbulence generates vortices and fluid
50 velocity fluctuations down as far as the sub-millimetre scale²⁹, rendering fully-resolved simu-
51 lations computationally expensive, and necessitating state-of-the-art technologies such as
52 high-resolution fluorometry^{17,30} or underwater imaging³¹ for accurate experimental mea-
53 surements. Notwithstanding these difficulties, uncovering the mechanisms responsible for
54 widespread small-scale spatial patchiness remains essential, and in recent years, research
55 at the intersection of ecology and fluid dynamics has begun to present candidate mecha-
56 nisms^{32–34}.

57 In this paper, we address the key hypothesis that microbial motility interacts with mi-
58 croscale turbulence to trigger intense patchiness, increasing local microbe concentrations by
59 an order of magnitude or more^{32,35–37}. The aggregation effect has been hypothesised to be
60 driven by a coupling between fluid shear (which acts to overturn or ‘disorient’ swimmers) and
61 gyrotactic motility (by which the swimmers attempt to re-orient towards the vertical); when
62 a suitable balance is achieved between the overturning effect of shear, and the swimmers’
63 inherent stabilising torque, intense patchiness results³². So far however, this hypothesis has
64 been tested only in idealised isotropic turbulence regimes that are well-suited to mathemat-
65 ical analysis and simulation, but do not accurately reflect the turbulent environment that
66 microbes experience in, for example, lakes or oceans³⁷.

67 To overcome these limitations, we developed a novel, fully 3D microbe individual-based
68 model (IBM) resolved at the sub-metre scale and coupled with a direct numerical simulation
69 (DNS) of mixed-layer convective turbulence to simulate microbial spatial dynamics at a range
70 of depths. The use of an IBM allows us to resolve fine-scale spatial differences in fluid velocity
71 and its coupling with individual motility to recover the emergent spatial dynamics of microbes
72 and the formation of microscale patches. The fluid DNS reproduces density gradients that
73 drive spatial fluctuations in fluid buoyancy, to produce a realistic depth-varying anisotropic
74 turbulent flow. Seeding the flow with both non-motile and motile gyrotactic microbes tracked
75 using our IBM, we test whether the proposed mechanism of turbulence-driven patchiness
76 is realisable in flow regimes directly comparable to those that an aquatic microbe would
77 experience.

2 Results

2.1 Depth-structure of the simulated flow

Turbulence-driven patchiness is a complex function of microbial motility and the physical characteristics of the turbulent flow. Our simulation comprises an idealised ‘lab-scale’ model of oceanic or lacustrine mixing, in which the turbulence in the mixed layer is driven by cooling from the surface (full details in Methods Section 4.1) during the night, during the autumn or winter, or during a cold-air outbreak. The relative fluid density (ρ'/ρ_0), the turbulent kinetic energy (k) and the rate of turbulent energy dissipation (ϵ) vary with depth and have a weak dependence on time due to deepening of the mixed layer (Fig. 1). In particular, turbulence peaks just below the surface of the fluid, and steadily declines with depth before rapidly falling to zero when it approaches the density interface between $0.10 \text{ m} < z < 0.17 \text{ m}$. Below the interface, the fluid is quiescent. We thus expect the dynamics of the microbes to depend on depth. In order to determine the effect of these depth-varying turbulent conditions on microbial patchiness, we divided the parts of the simulation space into which microbes were seeded (Methods Section 4.2.2) into three distinct depth regions: ‘Shallow’ ($0.30 \text{ m} \geq z \geq 0.24 \text{ m}$), ‘Mid’ ($0.24 \text{ m} > z \geq 0.17 \text{ m}$) and ‘Deep’ ($0.17 \text{ m} > z \geq 0.10 \text{ m}$), as shown in Fig. 1, and separately analysed patchiness in each depth region.

2.2 Gyrotactic motility and microbe patchiness within the simulated flow

We investigated whether and how turbulent fluid motion can drive substantial increases in patchiness through a coupling of vortical fluid shear and gyrotactic microbial motility. This process requires a balance between the intensity of the turbulent fluid motion and the ‘agility’ of the microbes – their swimming speed and ability to re-orient towards the vertical. We tested whether this balance is, in practice, achievable for microbes in a realistic turbulent environment by introducing, into the flow, virtual non-motile and motile microbe populations spanning a range of two key biological parameters for gyrotactic motility; swimming velocity v_{swim} and reorientation timescale B (Methods Section 4.2.2) in life-like concentrations

105 and tracking their motion through the fluid (Methods Section 4.2, Fig. 2, Supplementary
 106 Movie 1). We quantified patchiness using the “patch concentration enhancement factor” Q
 107 (Methods Section 4.3) to compare motile and non-motile microbe accumulation into patches.
 108 Q is dimensionless, and captures the difference in patch concentration between motile and
 109 non-motile microbes; positive Q -values indicate that motile microbes are more concentrated
 110 within patches than non-motile microbes and vice-versa. More precisely, since patches are
 111 constantly forming and dissipating in the turbulent flow, Q captures the tendency of motile
 112 microbes to spend time in regions where the population density is Q -fold greater than that of
 113 a non-motile population. Comparing the patchiness of the different virtual microbe popula-
 114 tions, we found that ‘agile’ motile microbes with fast swim speed ($100\text{--}500\ \mu\text{m s}^{-1}$) and quick
 115 reorientation timescale ($1\text{--}3\ \text{s}$) respond differently to turbulence than do ‘non-agile’ microbes
 116 of low or intermediate swim speed ($10\text{--}100\ \mu\text{m s}^{-1}$) and slow reorientation timescale ($3\text{--}5\ \text{s}$)
 117 (Fig. 3).

118 Non-agile motile microbes exhibited little variation in patchiness enhancement at different
 119 depths (Fig. 3a,c,e). In these populations, patchiness enhancement troughed/peaked around
 120 $Q = -0.4/+0.4$ in the Shallow and Mid regions and at about $Q = -0.7/+0.8$ in the Deep
 121 region, but average enhancement, \bar{Q} , was near zero in all three regions, meaning that little
 122 mean difference in patchiness was found between these motile microbes and their non-motile
 123 counterparts. We note that, although the differences are small, enhancement was generally
 124 positive ($\bar{Q}_{\text{deep}} > 0$) in the Deep region of the simulation, but negative ($\bar{Q}_{\text{mid}} < 0$ and
 125 $\bar{Q}_{\text{shallow}} < 0$) in the Mid and Shallow regions.

126 More agile motile microbes exhibited stronger (positive and negative) patchiness enhance-
 127 ment (Fig. 3b,d,f). Q -values troughed/peaked around $Q = -0.6/+0.4$ in the ‘Shallow’ and
 128 ‘Mid’ regions, and troughed/peaked around $Q = -0.8/+1.6$ in the ‘Deep’ region. Although
 129 stronger than in non-agile microbes, average patch enhancement in the ‘Shallow’ and ‘Mid’
 130 regions remained weak and negative, and was again positive and strongest in the ‘Deep’
 131 region.

132 Overall, two clear trends emerged from this analysis (Fig. 4). Firstly, we saw a clear dif-
 133 ference between patch enhancement in the Shallow–Mid regions and in the Deep region, with
 134 the former generally (and unexpectedly) exhibiting very weak negative patch enhancement

135 ($\overline{Q}_{\text{shallow}} < 0$, $\overline{Q}_{\text{mid}} < 0$) and the latter exhibiting positive patch enhancement ($\overline{Q}_{\text{deep}} > 0$).
 136 Secondly, only the most agile motile microbes, sustaining both high swim speeds and fast
 137 reorientation timescales, achieved a significant difference in patchiness from their non-motile
 138 cousins ($|Q| \geq 1$), but then only transiently and in the Deep region. With reductions in swim
 139 speed came substantial falls in mean patchiness enhancement ($|\overline{Q}| \leq 0.07$) (Supplementary
 140 Figs. 4–6).

141 How are the differences in motility in our simulated microbes interacting with turbulence
 142 to stimulate or hinder patchiness in each depth region? Our gyrotactic microbes migrate
 143 vertically through the flow through the combined action of two concurrent processes – vertical
 144 advection in falling or rising regions of fluid, and individual locomotion by the microbes
 145 themselves. At the level of individual locomotion, microbes experience a constant battling
 146 of forces between the viscous torque exerted on them by shear in the surrounding fluid
 147 and the stabilising torque (represented by the reorientation timescale parameter B in our
 148 simulations) which reorients the microbes towards the upwards vertical direction. This is
 149 reflected in the orientations of the microbes relative to the vertical in our simulations (Fig.
 150 5); microbes with low B -value reorient quickly, and are thus more frequently able to overcome
 151 viscous torque to orient themselves “upwards”, whereas microbes with higher B -values are
 152 slow to reorient and more vulnerable to “disorientation” due to viscous torque. We note that
 153 swim speed did not appear to impact the distribution of microbe orientations.

154 Microbe orientation alone is only part of the story underlying the patchiness trends
 155 described above; changes in the spatial distribution of microbes in our simulated flow result
 156 from the combined effects of individual swimming dynamics and vertical advection by the
 157 flow itself. This is particularly important in a highly variegated flow such as our turbulent
 158 DNS, wherein local fluid velocities can vary from near-zero to ~ 2 orders of magnitude
 159 above a microbe’s swimming velocity, depending on the microbe in question and its location
 160 within the flow. To investigate this combined effect, we computed the ‘effective velocity’
 161 (v_{eff}) of our microbes – the sum of the instantaneous motion of the fluid surrounding a
 162 microbe and the microbe’s swimming velocity at that moment. We computed the effective
 163 velocity in spherical coordinates $v_{\text{eff}} = (|v_{\text{eff}}|, \theta_{\text{eff}}, \phi_{\text{eff}})$ since this more naturally yields the
 164 magnitude $|v_{\text{eff}}|$ (“effective speed”) and polar component θ_{eff} (“effective polar orientation”) of

165 the microbes. In particular, the polar component θ_{eff} captures the tendency of microbes to
166 alter their depth within the simulated fluid, unlike the microbe orientation, which does not
167 account for the movement of the surrounding fluid. Similarly, the magnitude of the effective
168 velocity captures the speed at which microbes can move through the simulated space, not just
169 their motion relative to that of the surrounding fluid. Within each simulation we compute
170 effective velocities for all microbes every 1 second from $t = 20\text{--}60$ s. Since both the velocity
171 and vorticity of our simulated fluid are highly depth-dependent, we expect v_{eff} to exhibit
172 strong depth-dependency as well, and as such we analyse v_{eff} separately in the Shallow, Mid
173 and Deep regions.

174 Within the Shallow (Fig. 6a,b) and Mid (Fig. 6c,d) regions, effective velocities exhibit lit-
175 tle variation between simulations, with both the polar angle and the magnitude of effective
176 velocity remaining relatively constant across the full range of B and v_{swim} parameter values.
177 In the Deep region (Fig. 6e,f), the polar angle is approximately horizontal but again exhibits
178 little variation between simulations, while the magnitude varies by a margin ($\sim 13 \text{ mm s}^{-1}$)
179 significantly greater than the largest difference in microbe swim speeds between simulations
180 (0.49 mm s^{-1}). Overall, with increasing depth, effective velocity slows and becomes increas-
181 ingly horizontal, with microbes in the ‘Deep’ region moving near-horizontally.

182 **3 Discussion**

183 Microscale microbe patchiness may have far-reaching implications both for the microbes
184 themselves and for the wider ecosystem, but it is first and foremost essential to accurately
185 understand the prevalence and intensity of such patchiness in real-world conditions. By
186 combining state-of-the-art individual-based modelling tools with a realistic 3D model of tur-
187 bulence, we have shown that patchiness driven by the interaction of turbulence and gyrotactic
188 motility is likely to be modest in intensity, and limited in practise to particularly agile motile
189 microbes and to deeper regions of the mixed layer where convective turbulence is less intense
190 than at the surface.

191 Although our DNS simulates only a relatively small physical volume of water, physical
192 scaling arguments (see SI Section 2) establish limits on the differences in turbulent fluid

193 motion between our DNS and in larger real-world flows. Turbulent velocity fluctuations
194 in the ocean mixed layer are between 0.93 – 7.88-fold stronger than in our DNS, while we
195 could not find sufficient data to compare our DNS to mixed layer turbulence in lakes. These
196 scaling relationships allow us to extrapolate the effects of turbulence on microbial patchiness
197 within our simulated flow to comparable oceanic conditions (see below and Supplementary
198 Methods 2). Future efforts to model microscale spatial activity in realistic oceanic flow
199 regimes, including turbulence, would benefit from detailed empirical measurements of how
200 turbulent fluid velocity fluctuations vary from small-scale volumes such as our DNS, to real-
201 world scenarios such as the marine water column. This could substantially simplify the
202 process of determining how to interpret the results and predictions of scaled-down models
203 to real-world systems.

204 Convective overturning is a key driver of mixed-layer turbulence^{38–40}. Our buoyancy-
205 driven DNS reproduces convective mixing driven by heat loss from the fluid surface (Results
206 Section 2.1). Comparable oceanic conditions are most commonly associated with the mid-
207 latitudes, though particularly strong and deep convection can also occur in sub-polar regions
208 such as the Labrador and Greenland seas⁴¹. Surface cooling varies both daily, with the solar
209 cycle, and seasonally, with oceans in particular acting as heat reservoirs during autumn and
210 winter⁴². Our simulations are therefore best interpreted in the context of a body of water
211 undergoing convective mixing due to heat loss to the atmosphere during autumnal or winter
212 cooling, during the night, or during a cold-air outbreak^{43,44}. Our results suggest that in a
213 convective mixed-layer, turbulent fluid motion near the surface of the fluid will greatly exceed
214 the locomotive capabilities of gyrotactic microbes, inhibiting patch enhancement. Farther
215 from the fluid surface, turbulence becomes relatively weak, analogously to the region near
216 or below the thermocline in a real body of water. At these relatively quiescent depths,
217 highly agile microbes can attain the balance of viscous and stabilising torques that drives
218 modest ($Q \approx 1.6$) patch enhancement. In oceanic flows with particularly strong surface
219 cooling (and hence a deeper mixed-layer), turbulent velocity fluctuations can be up to 7.88-
220 fold stronger than in our simulation (see again SI Section 2), and patch enhancement may
221 be especially difficult to achieve. It must also be stressed that the ocean mixed layer is
222 not constantly overturning, but also undergoes periods of minimal or negative heat loss

223 through the surface, when our turbulence regime is not applicable. Due to computational
224 constraints, we have not modelled the effects of other sources of turbulence, such as wind or
225 waves. We predict that, since turbulence from these sources would also be strongest near the
226 fluid surface and decline with depth, our results would not qualitatively change with their
227 inclusion; additional turbulence near the fluid surface would continue to disperse microbe
228 patches, while at greater depth, highly motile microbes may begin to form patches through
229 coupling with weaker turbulence.

230 Our analysis of the “effective velocities” of our simulated microbes is consistent with the
231 hypothesis³² that positive patch enhancement is caused by the interaction of turbulent fluid
232 vorticity and the stabilising torque of the gyrotactic microbes themselves. In regions of
233 positive patch enhancement, the net effect of these competing forces is to constrain average
234 microbe movement to a nearly horizontal direction (Fig. 6e,f). This may be the proximate
235 cause of positive mean patch enhancement; with the vertical dimension effectively denied to
236 them, microbes must move in an horizontal sub-space, increasing local concentrations within
237 that subspace relative to unconstrained non-motile microbes. How might microbes escape
238 such regions of a flow, or indeed enter them in the first place? Fig 7c shows that the packets
239 of upwelling and downwelling fluid that are characteristic of buoyancy-driven turbulent flows
240 can penetrate into the ‘Deep’ region of the flow (albeit in a weakened form relative to the
241 surface). This suggests that microbes may ‘hitch’ a ride in vertically-moving packets of fluid,
242 thereby transiting from high-turbulence to low-turbulence regions (or vice-versa) much more
243 rapidly than their locomotion alone would allow them to. This is supported by an analysis
244 of microbe vertical displacement over the course of our simulations; almost all microbes
245 (> 90%) in each simulation traversed at least one full depth region (70 mm) during the full
246 60 s, whereas in a static fluid, even the fastest swimmers ($v_{\text{swim}} = 500 \mu\text{m s}^{-1}$) swimming in a
247 straight vertical line would have covered no more than 30 mm. Supplementary Fig. 8 shows
248 the depth trajectories of samples of both agile and non-agile microbes, which exhibit large
249 vertical movements corresponding to advection in upwelling or downwelling packets of fluid,
250 and longer periods of residence in the deeper, more quiescent region.

251 Finally, our results raise interesting questions about the utility of gyrotactic locomotion
252 in different turbulent conditions. In the presence of strong turbulence in particular, increased

253 agility has little effect on the effective velocity of a microbe (Fig. 6a–d), and only a very weak
254 (and negative) effect on patch enhancement (Fig. 4). In more quiescent waters, we saw up to
255 a 2-fold difference between the effective speeds ($|v_{\text{eff}}|$) of fast and slow swimmers. The most
256 likely mechanism for this large increase in effective speed is that fast swimmers are more
257 efficient than their slower-swimming counterparts at encountering and remaining within fast-
258 moving packets of fluid, allowing these fast microbes to boost their effective velocity by up
259 to 12 mm s^{-1} – an increase well beyond the physiological capabilities of microbial motility
260 alone^{45,46}. Furthermore, motile microbes are known to modify their swim speed in response
261 to environmental stimuli such as temperature⁴⁷, nutrient concentration gradients^{48,49}, and
262 even turbulence^{50,51}, and thus could strategically vary their agility in response to local fluid
263 and environmental conditions. For example, microbes in modest, patch-enhancing turbu-
264 lence could downregulate swim speed to decrease patchiness and reduce predation²¹ or viral
265 infection risks^{22,23}, and microbes in shallower, nutrient-poor waters could temporarily up-
266 regulate swimming speed in order to improve their chances of entering a downwell towards
267 deeper waters where nutrients are typically more plentiful⁵².

268 Even if microbes do not dynamically tune their motility in turbulence in search of tempo-
269 rary individual advantages over their competitors and environment, our results demonstrate
270 that turbulence-driven microscale patchiness in real-world conditions is a delicate balancing
271 act of physical fluid conditions and individual motility, and not a ubiquitous consequence
272 of gyrotaxis. There is much scope for further individual-based modelling at these scales to
273 further expand our understanding of the interactions at play; for example by extending our
274 model to include dynamic tuning of motility at the individual microbe level, or by incor-
275 porating additional trophic levels such as nutrients or predation. The longevity of patches,
276 when they do occur, is a key additional component of their ecological importance; in order
277 for microbe patches to affect reproduction or nutrient distributions, for example, the lifetime
278 of a patch cannot be smaller than the timescale of reproduction or of resource consumption⁹.
279 Since we do not currently have the tools to reliably determine patch lifetimes for compari-
280 son between simulations, we are not able to report patch lifetimes for the results from this
281 study. Modelling or measuring in-situ the longevity of microbe patches, and their longevity’s
282 dependence on conditions such as turbulence, will be critical to future research in this space.

283 4 Methods

284 Our microbe simulations consist of a series of experiments in a fully resolved lab-scale sim-
285 ulation of convective mixing due to surface cooling in a two-layer stratified flow. Each
286 experiment targeted a different combination of biological parameters controlling the motility
287 of the microbes, in order to test the predictions of earlier work and understand how sensitive
288 patchiness is to motility parameters. In this section we give details of the fluid simulation,
289 the microbe IBM and the algorithms used to quantify patches and patchiness.

290 4.1 Direct simulation of a mixed layer driven by convection

291 The flow targeted in this paper is convection in the top-layer of a two-layer stratified fluid
292 due to surface cooling. These flows are of direct relevance to the oceanic mixed layer and
293 convective mixing in lakes³⁸⁻⁴⁰. As we aim to simulate the behaviour of microbes, it is
294 essential that all dynamic scales of the turbulence are resolved. This implies (1) that a
295 highly accurate code for direct numerical simulation needs to be employed; and (2) that
296 the problem should be scaled down to a lab-scale, since it is impossible to resolve all the
297 turbulence at real-world oceanic or lacustrine scales.

298 The domain is $0.6 \times 0.6 \times 0.3$ m (length \times width \times height), and the fluid inside the domain
299 comprises two layers of thickness $h_0 = 0.15$ m of which the top layer has a density that is
300 75% lower than that of the bottom layer, thus creating a stable stratification. The density
301 jump used here is much stronger than in lakes or the ocean, but is chosen to limit turbulent
302 entrainment and thus slow down the deepening of the mixed layer⁵³. The strength of the
303 density jump does not significantly affect the turbulent flow in the mixed layer, except very
304 close to the interface, where we do not seed particles in the microbe simulations. The fluid
305 is subjected to a negative buoyancy flux B at the top of the domain, which is representative
306 of the cooling of the water surface due to long wave radiation during night time, winter or
307 autumn cooling, or during a cold-air outbreak. As a result, the fluid near the surface cools
308 and begins to descend, forming a convective mixed layer above the density interface.

309 In order to be able to resolve all the turbulent scales of motion, a kinematic viscosity
310 $\nu = 5 \times 10^{-6} \text{m}^2 \text{s}^{-1}$ was chosen, which is slightly higher than that of water. A thermal

311 diffusivity was set to $4 \times 10^{-6} \text{m}^2 \text{s}^{-1}$. Setting the buoyancy flux $B = 5 \times 10^{-4} \text{m}^2 \text{s}^{-3}$ implies
 312 a characteristic velocity scale of the mixed layer $w_* = (Bh_0)^{1/3} = 0.042 \text{m s}^{-1}$ ^{54,55} (see Sup-
 313 plementary Methods). This implies that the initial bulk Richardson number and Reynolds
 314 number are:

$$315 \quad Ri_0 = \frac{h_0 \Delta b}{w_*^2} = 85, \quad Re = \frac{w_* h_0}{\nu} = 1260. \quad (1)$$

315 The computational grid is $720 \times 720 \times 360$, which corresponds to 186,624,000 cubic
 316 cells. Cell side-lengths are thus $\Delta x = \Delta y = \Delta z \approx 0.83 \text{mm}$. The dissipation rate peaks
 317 at $\epsilon = 2.66 \times 10^{-4} \text{m}^2 \text{s}^{-3}$ (see Fig. 1), which implies that the Kolmogorov scale is $\eta_K =$
 318 $(\nu^3/\epsilon)^{1/4} = 0.828 \text{mm}$. This is the size of the smallest turbulent eddy that is encountered in
 319 the flow. Since $\Delta x/\eta_K \approx 1$, it follows that all the turbulent scales of the flow are resolved,
 320 and the simulation can indeed be considered DNS.

321 At $t = 0 \text{s}$, the fluid is quiescent, after which the buoyancy flux is switched on. The total
 322 simulation time is 90 s, of which the first 30 s are ‘spin-up’ time, in which the convective
 323 mixed layer is formed. The microbe simulations commence after these initial transients, and
 324 will thus only use the data for $30 \leq t \leq 90 \text{s}$.

325 The velocity and density fields are obtained using the direct numerical simulation code
 326 SPARKLE, which employs a symmetry-preserving fourth-order-accurate finite volume dis-
 327 cretization scheme, preserving mass, momentum and energy^{56,57}. SPARKLE solves the
 328 Navier-Stokes equations in 3D in the Boussinesq approximation:

$$\begin{aligned} \nabla \cdot \mathbf{u} &= 0, \\ \frac{\partial \mathbf{u}}{\partial t} + \nabla \cdot (\mathbf{u} \otimes \mathbf{u}) &= -\nabla p + \nu \nabla^2 \mathbf{u} + b \mathbf{k}, \\ \frac{\partial b}{\partial t} + \nabla \cdot (\mathbf{u} b) &= \kappa \nabla^2 b, \end{aligned} \quad (2)$$

329 where space is denoted as $\mathbf{x} = (x, y, z)$ and fluid velocity by $\mathbf{u} = \mathbf{u}(\mathbf{x}) = (u(\mathbf{x}), v(\mathbf{x}), w(\mathbf{x}))$,
 330 p is kinematic pressure, ν is kinematic viscosity, $b = b(\mathbf{x}, t)$ is buoyancy, κ is thermal dif-
 331 fusivity and \mathbf{k} is the unit vector in the z -direction. The buoyancy $b(\mathbf{x}, t)$ is given by a

332 linear equation of state $b = \beta g \theta$, where $\beta = -T_0^{-1} \partial \rho / \partial T|_{T_0}$ is the expansion coefficient, g
 333 is the gravitational acceleration and $\theta = T - T_0$ is the temperature relative to the reference
 334 temperature T_0 .

335 4.2 Gyrotactic Microbe IBM

336 Since aquatic environments are in constant motion, microbial ecosystems involve many in-
 337 herently Lagrangian processes that are well-suited to individual-based models (IBMs). IBMs
 338 are particularly well-suited to explicitly modelling 3D aquatic ecosystems in complex flow
 339 regimes, wherein agents must interact individually with their local environment (a turbu-
 340 lent eddy, for instance, or a nutrient patch), and/or with each other, and where complex
 341 ecosystem dynamics can emerge naturally from the collective behaviour of individuals in the
 342 model. IBMs of this kind have already seen active service in ecological research pertaining to
 343 questions as diverse as microbial patchiness³² and evolutionary dynamics⁵⁸, spatial dynamics
 344 of fish⁵⁹, fish larvae⁶⁰ and sea turtle hatchlings⁶¹, thermal responses in phytoplankton popu-
 345 lations⁶² and the dynamics of ocean plastics⁶³⁻⁶⁵. Here we describe the mathematical frame-
 346 work of our microbial motility model and its implementation using the OceanParcels^{66,67}
 347 Lagrangian analysis toolkit.

348 4.2.1 Gyrotactic Microbes as Bottom-Heavy Spheres

349 We model gyrotactic microbes as spheres with off-set centres of gravity, such that they
 350 passively align with the vertical in the absence of any external forces (gyrotaxis). Microbial
 351 movement is then modelled as two concurrent processes – advection by the turbulent flow,
 352 and individual locomotion in the instantaneous swimming direction. The re-orientation of
 353 microbes under turbulence and their subsequent re-alignment with the vertical is governed
 354 by the following equation⁶⁸:

$$\frac{d\mathbf{p}}{dt} = \frac{1}{2B} [\mathbf{k} - (\mathbf{k} \cdot \mathbf{p})\mathbf{p}] + \frac{1}{2}(\boldsymbol{\omega} \times \mathbf{p}), \quad (3)$$

355 where \mathbf{p} is a unit vector describing the swimming direction, $\boldsymbol{\omega} = \nabla \times \mathbf{u}$ is the fluid vorticity
 356 (curl of the velocity field), $\mathbf{k} = (0, 0, 1)$ is the unit vector in the positive vertical direction,

357 and B is the ‘gyrotactic reorientation timescale’ describing the typical time required for a
 358 disoriented cell to return to vertical alignment if $\boldsymbol{\omega} = 0$. Under this framework, the first
 359 term on the RHS encodes a microbe’s reorientation towards the vertical, while the second
 360 term encodes the ‘overturning’ effect of turbulence on the microbe, due to viscous torque.
 361 Microbe swimming velocities and gyrotactic reorientation timescales (B) are set as constant
 362 within each simulation, in order to test the sensitivity of patch formation to these biological
 363 parameters.

364 4.2.2 OceanParcels – computing microbe trajectories

365 We compute motile and non-motile particle trajectories using the OceanParcels Lagrangian
 366 particle tracking engine. Velocity fields are pre-computed in SPARKLE and fed to Ocean-
 367 Parcels (version 2.1.4) as netCDF4 files. We do not consider the physical effects of microbes
 368 on the flow. Using OceanParcel’s “custom kernel” functionality we track the microbes by
 369 integrating the per-microbe velocity associated with the superposition of the microbial swim-
 370 ming and the flow at each timestep:

$$\frac{d\mathbf{X}}{dt} = \mathbf{p}v_{\text{swim}} + \mathbf{u}(\mathbf{X}), \quad (4)$$

371 where \mathbf{X} is the microbe’s position, v_{swim} is the swimming velocity of the microbe and once
 372 again \mathbf{p} is its swimming direction and \mathbf{u} is the fluid velocity. This approach has previously
 373 been shown to accurately capture the trajectories of passive and active swimmers in a turbu-
 374 lent flow³². The microbe positions \mathbf{X} are integrated with an RK4 method, and the swimming
 375 directions \mathbf{p} are integrated with a Forward Euler method. All simulation outputs are stored
 376 in the netCDF4 file format.

377 In each simulation, 100,000 microbes were initialised at random positions within the
 378 upper half ($z \geq 0.15$ m) of the DNS flow, and with a random swimming direction. Periodic
 379 boundary conditions were applied in the horizontal directions, as in the DNS, and a reflective
 380 boundary condition was applied to the top (surface) boundary. Each simulation ran from
 381 the end of the DNS spin-up period to the end of the DNS (60 s in total), with a timestep
 382 of $\Delta t = 0.01$ s. The choice of timestep is discussed in detail in SI Section 1. We recorded

Table 1: OceanParcels simulation parameters.

Parameter	Units	Value
Dimensions	m	$0.6 \times 0.6 \times 0.3$
Total time	s	60
Δt	s	0.01
$n_{\text{particles}}$	–	100,000
B	s	1.0, 3.0 or 5.0
v_{swim}	$\mu\text{m s}^{-1}$	10, 100 or 500

the position and swimming direction of each microbe every 0.1s. Values for the parameters B and v_{swim} were chosen to span the range of values for these parameters estimated in the existing literature^{69–71}. Table 1 summarises the parameters for the OceanParcels simulations.

4.3 Quantifying Patchiness

4.3.1 Voronoi tessellation

In order to obtain a diagnostic for the local microbe concentration, we performed a 3D Voronoi tessellation of the microbe positions every second using the Voropp package (version 0.4.5), applying the same double horizontally periodic boundary conditions as the simulations and specifying upper ($z = 0.3$ m) and lower ($z = 0$ m) boundaries as in the simulated space. The Voronoi tessellation assigns to each microbe the polyhedral containing all points in the simulated space that are closer to that microbe than any other. The inverse of the volume of this polyhedral gives a measure of the local microbe concentration within that polyhedral.

4.3.2 Q -statistic

To quantify patchiness in our simulations, we first performed the 3D Voronoi tessellation described above. Then, following the approach outlined in³², we defined patches to consist of the fraction f of microbes with the largest local concentration (i.e. smallest Voronoi polyhedron volume), and we used the concentrations within these patches to calculate, at

400 every second, the ‘patch concentration enhancement factor’ Q :

$$Q = \frac{C - C_P}{C_M}, \quad (5)$$

401 where C is the median concentration among motile microbes inside patches, C_P is the median
402 concentration among non-motile particles inside patches, and C_M is a normalisation factor
403 equal to the overall concentration of microbes in each simulation. Q is thus dimensionless,
404 and captures the difference in patch concentration between motile and non-motile microbes;
405 positive Q -values indicate that motile microbes are more concentrated within patches than
406 non-motile microbes and vice-versa. For the results reported in this paper, we chose $f = 0.01$
407 so that our patches consist of the 1% most-concentrated microbes. We note that our use of a
408 reflective boundary condition at the upper boundary of the fluid simulation may not reflect
409 the true dynamics of gyrotactic particles at the very surface of a fluid, and we therefore do
410 not include microbes residing in the top-most DNS cell layer ($0.2991\overline{66} \text{ m} < z \leq 0.3 \text{ m}$) in
411 the Q -analysis.

412 5 Data Availability

413 The turbulent velocity fields generated by SPARKLE and fed to the microbe individual-based
414 model are not hosted on a public repository due to filesize limitations ($\sim 2\text{TB}$ in total), but
415 are available upon request from the corresponding authors.

416 The outputs of the microbial individual-based model are not hosted on a public repos-
417 itory due to filesize limitations ($\sim 82\text{GB}$ in total), but are available upon request from the
418 corresponding authors.

419 6 Code availability

420 OceanParcels code is publicly available at <https://oceanparcels.org/index.html>. Our
421 microbe individual-based model ran on top of OceanParcels v2.1.4 (Github commit hash
422 ceb0e42b69046bc6dcb6540ac08268db1855f1e2). All original code pertaining to the microbe
423 individual-based model is available on Github at:

424 <https://github.com/christensen5/turbulence-patchiness-sims/tree/turbulence-patchiness->
425 [paper.](https://github.com/christensen5/turbulence-patchiness-sims/tree/turbulence-patchiness-)

426 References

- 427 1. Bar-On, Y. M., Phillips, R. & Milo, R. The Biomass Distribution on Earth. *Proceedings*
428 *of the National Academy of Sciences* **115**, 6506–6511 (2018).
- 429 2. Moran, M. A. The Global Ocean Microbiome. *Science* **350**, aac8455 (2015).
- 430 3. Falkowski, P. G., Fenchel, T. & Delong, E. F. The Microbial Engines That Drive Earth’s
431 Biogeochemical Cycles. *Science* **320**, 1034–1039 (2008).
- 432 4. Field, C. B., Behrenfeld, M. J., Randerson, J. T. & Falkowski, P. Primary Production of
433 the Biosphere: Integrating Terrestrial and Oceanic Components. *Science* **281**, 237–240
434 (1998).
- 435 5. Azam, F. *et al.* The Ecological Role of Water-Column Microbes in the Sea. *Marine*
436 *Ecology Progress Series* **10**, 257–263 (1983).
- 437 6. Ducklow, H. W. & Carlson, C. A. in *Advances in Microbial Ecology* 113–181 (Springer
438 Boston, 1992). ISBN: 978-1-4684-7611-8.
- 439 7. Smith, D. C., Simon, M., Alldredge, A. L. & Azam, F. Intense Hydrolytic Enzyme
440 Activity on Marine Aggregates and Implications for Rapid Particle Dissolution. *Nature*
441 **359**, 139–142 (1992).
- 442 8. Gifford, S. M., Sharma, S., Rinta-Kanto, J. M. & Moran, M. A. Quantitative Analysis
443 of a Deeply Sequenced Marine Microbial Metatranscriptome. *The ISME Journal* **5**,
444 461–472 (2011).
- 445 9. Siegel, D. A. Resource Competition in a Discrete Environment: Why Are Plankton
446 Distributions Paradoxical? *Limnology and Oceanography* **43**, 1133–1146 (1998).
- 447 10. Hardy, A. C. & Gunther, E. R. in *Discovery Reports* 1–456 (Cambridge University
448 Press, 1935).

- 449 11. Hardy, A. C. A Further Example of the Patchiness of Plankton Distribution. *Deep Sea*
450 *Research*: **3 (Suppl.)** 7–11 (1955).
- 451 12. Denman, K. L. & Platt, T. The Variance Spectrum of Phytoplankton in a Turbulent
452 Ocean. *Journal of Marine Research* **34**, 593–601 (1976).
- 453 13. Denman, K. L. & Powell, T. M. in *Oceanography and Marine Biology - An Annual*
454 *Review* 125–168 (1984).
- 455 14. Martin, A. P. Phytoplankton Patchiness: The Role of Lateral Stirring and Mixing.
456 *Progress in Oceanography* **57**, 125–174 (2003).
- 457 15. Mackas, D. L., Denman, K. L. & Abbott, M. R. Plankton Patchiness: Biology in the
458 Physical Vernacular. *Bulletin of Marine Science* **37**, 652–674 (1985).
- 459 16. Seymour, J. R., Mitchell, J. G. & Seuront, L. Microscale Heterogeneity in the Activity
460 of Coastal Bacterioplankton Communities. *Aquatic Microbial Ecology* **35**, 1–16 (2004).
- 461 17. Mitchell, J. G., Yamazaki, H., Seuront, L., Wolk, F. & Li, H. Phytoplankton Patch Pat-
462 terns: Seascape Anatomy in a Turbulent Ocean. *Journal of Marine Systems. Physical-*
463 *Biological Interactions in the Upper Ocean* **69**, 247–253 (2008).
- 464 18. Dann, L. M. *et al.* Microbial Micropatches within Microbial Hotspots. *PLOS ONE* **13**,
465 197–224 (2018).
- 466 19. Blackburn, N., Azam, F. & Hagström, Å. Spatially Explicit Simulations of a Microbial
467 Food Web. *Limnology and Oceanography* **42**, 613–622 (1997).
- 468 20. Kiørboe, T. & Jackson, G. A. Marine Snow, Organic Solute Plumes, and Optimal
469 Chemosensory Behavior of Bacteria. *Limnology and Oceanography* **46**, 1309–1318 (2001).
- 470 21. Deuer, S. M. & Grünbaum, D. Individual Foraging Behaviors and Population Distribu-
471 tions of a Planktonic Predator Aggregating to Phytoplankton Thin Layers. *Limnology*
472 *and Oceanography* **51**, 109–116 (2006).
- 473 22. Fuhrman, J. A. Marine Viruses and Their Biogeochemical and Ecological Effects. *Nature*
474 **399**, 541–548 (1999).

- 475 23. Seymour, J. R., Seuront, L., Doubell, M., Waters, R. L. & Mitchell, J. G. Microscale
476 Patchiness of Virioplankton. *Journal of the Marine Biological Association of the United*
477 *Kingdom* **86**, 551–561 (2006).
- 478 24. Tiselius, P. Behavior of Acartia Tonsa in Patchy Food Environments. *Limnology and*
479 *Oceanography* **37**, 1640–1651 (1992).
- 480 25. Brentnall, S. J., Richards, K. J., Brindley, J. & Murphy, E. Plankton Patchiness and Its
481 Effect on Larger-Scale Productivity. *Journal of Plankton Research* **25**, 121–140 (2003).
- 482 26. Long, R. A. & Azam, F. Microscale Patchiness of Bacterioplankton Assemblage Rich-
483 ness in Seawater. *Aquatic Microbial Ecology* **26**, 103–113 (2001).
- 484 27. Hutchinson, G. E. The Paradox of the Plankton. *The American Naturalist* **95**, 137–145
485 (1961).
- 486 28. Richerson, P., Armstrong, R. & Goldman, C. R. Contemporaneous Disequilibrium, a
487 New Hypothesis to Explain the „Paradox of the Plankton”. *Proceedings of the National*
488 *Academy of Sciences* **67**, 1710–1714 (1970).
- 489 29. Jiménez, J. in *Lectures on Plankton and Turbulence Scientia Marina* 61 (Supl. 1), 47–
490 56 (International Centre for Coastal Resources, Barcelona, 1997).
- 491 30. Yamazaki, H., Mitchell, J. G., Seuront, L., Wolk, F. & Li, H. Phytoplankton Microstruc-
492 ture in Fully Developed Oceanic Turbulence. *Geophysical Research Letters* **33** (2006).
- 493 31. Malkiel, E., Alquaddoomi, O. & Katz, J. Measurements of Plankton Distribution in
494 the Ocean Using Submersible Holography. *Measurement Science and Technology* **10**,
495 1142–1152 (1999).
- 496 32. Durham, W. M. *et al.* Turbulence Drives Microscale Patches of Motile Phytoplankton.
497 *Nature Communications* **4** (2013).
- 498 33. Barry, M. T., Rusconi, R., Guasto, J. S. & Stocker, R. Shear-Induced Orientational
499 Dynamics and Spatial Heterogeneity in Suspensions of Motile Phytoplankton. *Journal*
500 *of The Royal Society Interface* **12**, 20150791 (2015).
- 501 34. Schmidt, L., Fouxon, I., Krug, D., van Reeuwijk, M. & Holzner, M. Clustering of Par-
502 ticles in Turbulence Due to Phoresis. *Physical Review E* **93** (2016).

- 503 35. Kessler, J. O. Hydrodynamic Focusing of Motile Algal Cells. *Nature* **313**, 218–220
504 (1985).
- 505 36. Durham, W. M., Climent, E. & Stocker, R. Gyrotaxis in a Steady Vortical Flow. *Physical Review Letters* **106**, 238102 (2011).
506
- 507 37. Rusconi, R. & Stocker, R. Microbes in Flow. *Current Opinion in Microbiology. Environmental Microbiology - Extremophiles* **25**, 1–8 (2015).
508
- 509 38. Shay, T. J. & Gregg, M. C. Turbulence in an Oceanic Convective Mixed Layer. *Nature*
510 **310**, 282–285 (1984).
- 511 39. Marshall, J. & Schott, F. Open-Ocean Convection: Observations, Theory, and Models.
512 *Reviews of Geophysics* **37**, 1–64 (1999).
- 513 40. Read, J. S. *et al.* Lake-Size Dependency of Wind Shear and Convection as Controls on
514 Gas Exchange. *Geophysical Research Letters* **39** (2012).
- 515 41. Soloviev, A. & Klinger, B. in *Encyclopedia of Ocean Sciences* 2015–2022 (Elsevier,
516 2001). ISBN: 978-0-12-227430-5.
- 517 42. Kantha, L. & Clayson, C. A. in *Encyclopedia of Atmospheric Sciences* Second, 291–298
518 (Elsevier, 2003). ISBN: 978-0-12-382226-0.
- 519 43. Zikanov, O., Slinn, D. N. & Dhanak, M. R. Turbulent Convection Driven by Surface
520 Cooling in Shallow Water. *Journal of Fluid Mechanics* **464**, 81–111 (2002).
- 521 44. Smith, E. T. & Sheridan, S. C. Where Do Cold Air Outbreaks Occur, and How Have
522 They Changed Over Time? *Geophysical Research Letters* **47**, e2020GL086983 (2020).
- 523 45. Mitchell, J. G. *et al.* Long Lag Times and High Velocities in the Motility of Natural
524 Assemblages of Marine Bacteria. *Applied and Environmental Microbiology* **61**, 877–882
525 (1995).
- 526 46. Kamykowski, D., Reed, R. E. & Kirkpatrick, G. J. Comparison of Sinking Velocity,
527 Swimming Velocity, Rotation and Path Characteristics among Six Marine Dinoflagellate
528 Species. *Marine Biology* **113**, 319–328 (1992).
- 529 47. Kamykowski, D. & McCollum, S. A. The Temperature Acclimatized Swimming Speed
530 of Selected Marine Dinoflagellates. *Journal of Plankton Research* **8**, 275–287 (1986).

- 531 48. Stocker, R. & Seymour, J. R. Ecology and Physics of Bacterial Chemotaxis in the
532 Ocean. *Microbiology and Molecular Biology Reviews* **76**, 792–812 (2012).
- 533 49. Taylor, J. R. & Stocker, R. Trade-Offs of Chemotactic Foraging in Turbulent Water.
534 *Science* **338**, 675–679 (2012).
- 535 50. Sengupta, A., Carrara, F. & Stocker, R. Phytoplankton Can Actively Diversify Their
536 Migration Strategy in Response to Turbulent Cues. *Nature* **543**, 555–558 (2017).
- 537 51. Berdalet, E. *et al.* Species-Specific Physiological Response of Dinoflagellates to Quan-
538 tified Small-Scale Turbulence¹. *Journal of Phycology* **43**, 965–977 (2007).
- 539 52. Cullen, J. J. Diel Vertical Migration by Dinoflagellates: Roles of Carbohydrate Metabolism
540 and Behavioural Flexibility. *Contributions in Marine Science* **27(suppl.)** 135–152 (1985).
- 541 53. Fernando, H. J. S. Turbulent Mixing in Stratified Fluids. *Annual Review of Fluid Me-*
542 *chanics* **23**, 455–493 (1991).
- 543 54. Deardorff, J. W. Convective Velocity and Temperature Scales for the Unstable Plane-
544 tary Boundary Layer and for Rayleigh Convection. *Journal of the Atmospheric Sciences*
545 **27**, 1211–1213 (1970).
- 546 55. Rutgersson, A., Smedman, A. & Sahlée, E. Oceanic Convective Mixing and the Impact
547 on Air-Sea Gas Transfer Velocity. *Geophysical Research Letters* **38** (2011).
- 548 56. Craske, J. & van Reeuwijk, M. Energy Dispersion in Turbulent Jets. Part 1. Direct
549 Simulation of Steady and Unsteady Jets. *Journal of Fluid Mechanics* **763**, 500–537
550 (2015).
- 551 57. Verstappen, R. W. C. P. & Veldman, A. E. P. Symmetry-Preserving Discretization of
552 Turbulent Flow. *Journal of Computational Physics* **187**, 343–368 (2003).
- 553 58. Walworth, N. G., Zakem, E. J., Dunne, J. P., Collins, S. & Levine, N. M. Microbial
554 Evolutionary Strategies in a Dynamic Ocean. *Proceedings of the National Academy of*
555 *Sciences* **117**, 5943–5948 (2020).
- 556 59. McInnes, A. S. *et al.* Live Cell Analysis at Sea Reveals Divergent Thermal Performance
557 between Photosynthetic Ocean Microbial Eukaryote Populations. *The ISME Journal*
558 **13**, 1374 (2019).

- 559 60. Lindo-Atichati, D., Jia, Y., Wren, J. L. K., Antoniadou, A. & Kobayashi, D. R. Eddies
560 in the Hawaiian Archipelago Region: Formation, Characterization, and Potential Im-
561 plications on Larval Retention of Reef Fish. *Journal of Geophysical Research: Oceans*
562 **125**, e2019JC015348 (2020).
- 563 61. Le Gouvello, D. Z. M., Hart-Davis, M. G., Backeberg, B. C. & Nel, R. Effects of
564 Swimming Behaviour and Oceanography on Sea Turtle Hatchling Dispersal at the In-
565 tersection of Two Ocean Current Systems. *Ecological Modelling* **431**, 109130 (2020).
- 566 62. Kontopoulos, D.-G. *et al.* Phytoplankton Thermal Responses Adapt in the Absence of
567 Hard Thermodynamic Constraints. *Evolution* **74**, 775–790 (2020).
- 568 63. Sterl, M. F., Delandmeter, P. & van Sebille, E. Influence of Barotropic Tidal Currents
569 on Transport and Accumulation of Floating Microplastics in the Global Open Ocean.
570 *Journal of Geophysical Research: Oceans* **125**, e2019JC015583 (2020).
- 571 64. Wichmann, D., Delandmeter, P., Dijkstra, H. A. & van Sebille, E. Mixing of Passive
572 Tracers at the Ocean Surface and Its Implications for Plastic Transport Modelling.
573 *Environmental Research Communications* **1**, 115001 (2019).
- 574 65. Van Sebille, E. *et al.* Basin-Scale Sources and Pathways of Microplastic That Ends up
575 in the Galápagos Archipelago. *Ocean Science* **15**, 1341–1349 (2019).
- 576 66. Lange, M. & van Sebille, E. Parcels v0.9: Prototyping a Lagrangian Ocean Analysis
577 Framework for the Petascale Age. *Geoscientific Model Development Discussions*, 1–20
578 (2017).
- 579 67. Delandmeter, P. & van Sebille, E. The Parcels v2.0 Lagrangian Framework: New Field
580 Interpolation Schemes. *Geoscientific Model Development Discussions*, 1–24 (2019).
- 581 68. Pedley, T. J. & Kessler, a. J. O. Hydrodynamic Phenomena in Suspensions of Swimming
582 Microorganisms. *Annual Review of Fluid Mechanics* **24**, 313–358 (1992).
- 583 69. Jones, M. S., Baron, L. L. & Pedley, T. J. Biflagellate Gyrotaxis in a Shear Flow.
584 *Journal of Fluid Mechanics* **281**, 137–158 (1994).
- 585 70. Hill, N. A. & Häder, D. .-.-P. A Biased Random Walk Model for the Trajectories of
586 Swimming Micro-Organisms. *Journal of Theoretical Biology* **186**, 503–526 (1997).

587 71. Chen, X., Zeng, L., Wu, Y., Gao, Y. & Zhao, Y. Swimming Characteristics of Gyrotactic
588 Microorganisms in Low-Reynolds-Number Flow: *Chlamydomonas Reinhardtii*. *Energy,*
589 *Ecology and Environment* **2**, 289–295 (2017).

590 **Acknowledgements**

591 AKC is supported by the UK Natural Environment Research Council (NERC) through the
592 Quantitative Methods in Ecology and Evolution (QMEE) CDT, under grant NE/P012345/1.

593 MP acknowledges support from the UK Engineering and Physical Sciences Research Council
594 (EPSRC) under grant EP/R029423/1.

595 MvR would like to thank J.P. Mollicone for his assistance with the direct simulation reported
596 here, and acknowledges support from the UK turbulence consortium for computational re-
597 sources (EPSRC grant EP/R029326/1).

598 EvS is supported by the Dutch Research Council (NWO) through the ENW-Klein research
599 programme with project number OCENW.KLEIN.085

600 **Author Contributions**

601 AKC, SP, MP and EvS designed the study. MvR oversaw the generation of the direct
602 simulation data. AKC implemented and ran the microbe individual-based model in the
603 OceanParcels framework, with the assistance of MP and EvS. AKC performed the Voronoi
604 analysis, patchiness quantification, and analyses of the microbial trajectories, with the as-
605 sistance of MP and EvS. AKC and SP interpreted the results of the microbial model, with
606 input from EvS and MP. MvR and AKC conducted the Deardorff velocity scaling analysis.
607 AKC prepared the manuscript with input from all co-authors. SP, MP and EvS supervised
608 the project.

609 **Competing Interests Statement**

610 The authors declare no competing interests.

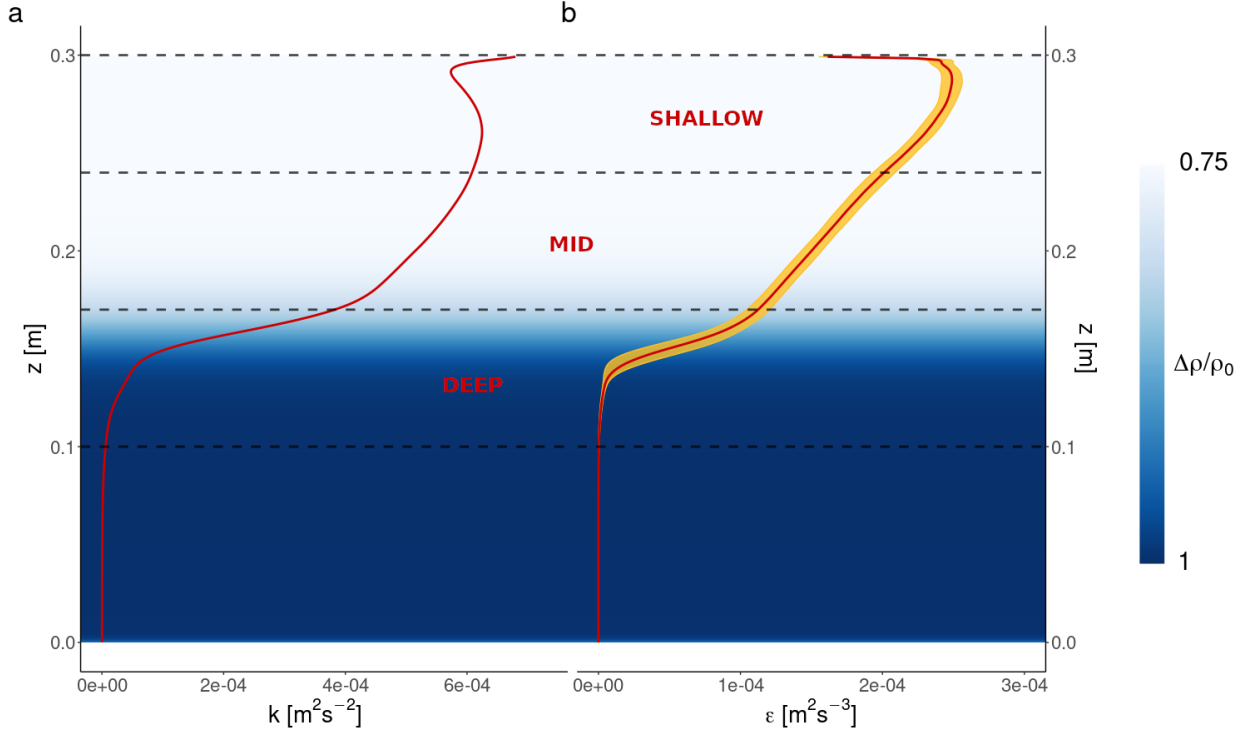


Figure 1: Depth structure of the simulated flow. The density of the fluid (relative to the reference density ρ_0 at $z = 0$) is represented by the white-blue gradient. **(a)** Turbulent kinetic energy (k) vs depth in the fluid DNS. The red line denotes the mean value of k at all simulated depths. **(b)** Turbulent dissipation rate (ϵ) vs depth in the fluid DNS. The red line denotes the mean value of ϵ at each simulated depth, while the golden ribbon shows the variance of ϵ at each depth. Variances are not known for panel (a) since k is itself computed from the variances of the fluid velocities. The “Shallow”, “Mid”, and “Deep” depth regions are labelled in red text and delimited by black dashed lines. Turbulence is strongest near the fluid surface and declines with depth, with essentially quiescent waters below the density interface.

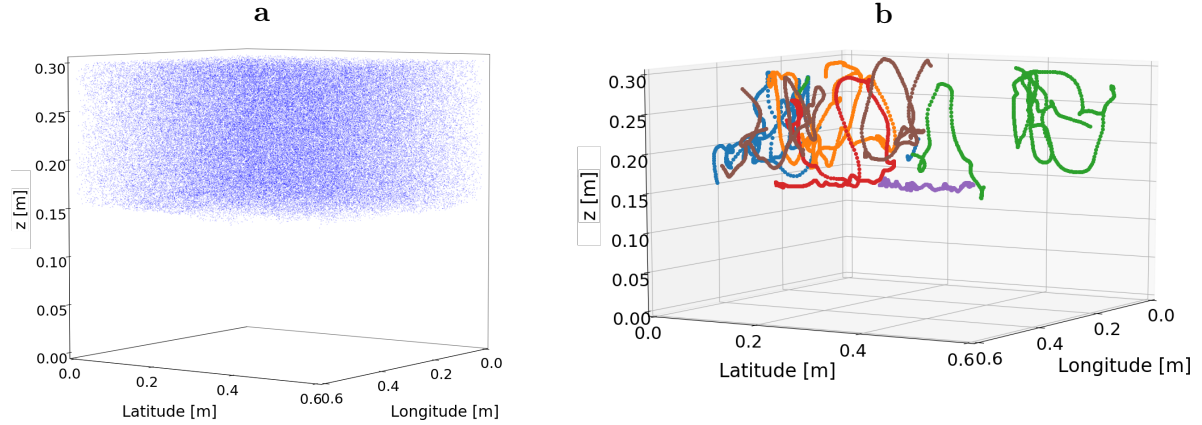


Figure 2: Microbial motion within the simulated flow. **(a)** A snapshot of microbe positions at $t = 25$ s of the $(B, v_{\text{swim}}) = (5 \text{ s}, 10 \mu\text{m s}^{-1})$ motile simulation. **(b)** Sample of six 3D microbe trajectories from $t = 0$ – 60 s in the $(B, v_{\text{swim}}) = (5 \text{ s}, 10 \mu\text{m s}^{-1})$ motile simulation. Each uniquely-coloured sequence of dots represents a single microbe’s trajectory. Owing to the periodic boundaries in the longitudinal and latitudinal directions, trajectories may appear discontinuous when a microbe moves through such a boundary (e.g. green trajectory). Microbes actively traverse the mixed layer, mostly due to rapid advection in upwelling or downwelling regions of fluid, but also through individual locomotion in less fast-moving regions of the fluid. In particular, long sojourns are noticeable at greater depths where turbulent fluid motion is less intense.

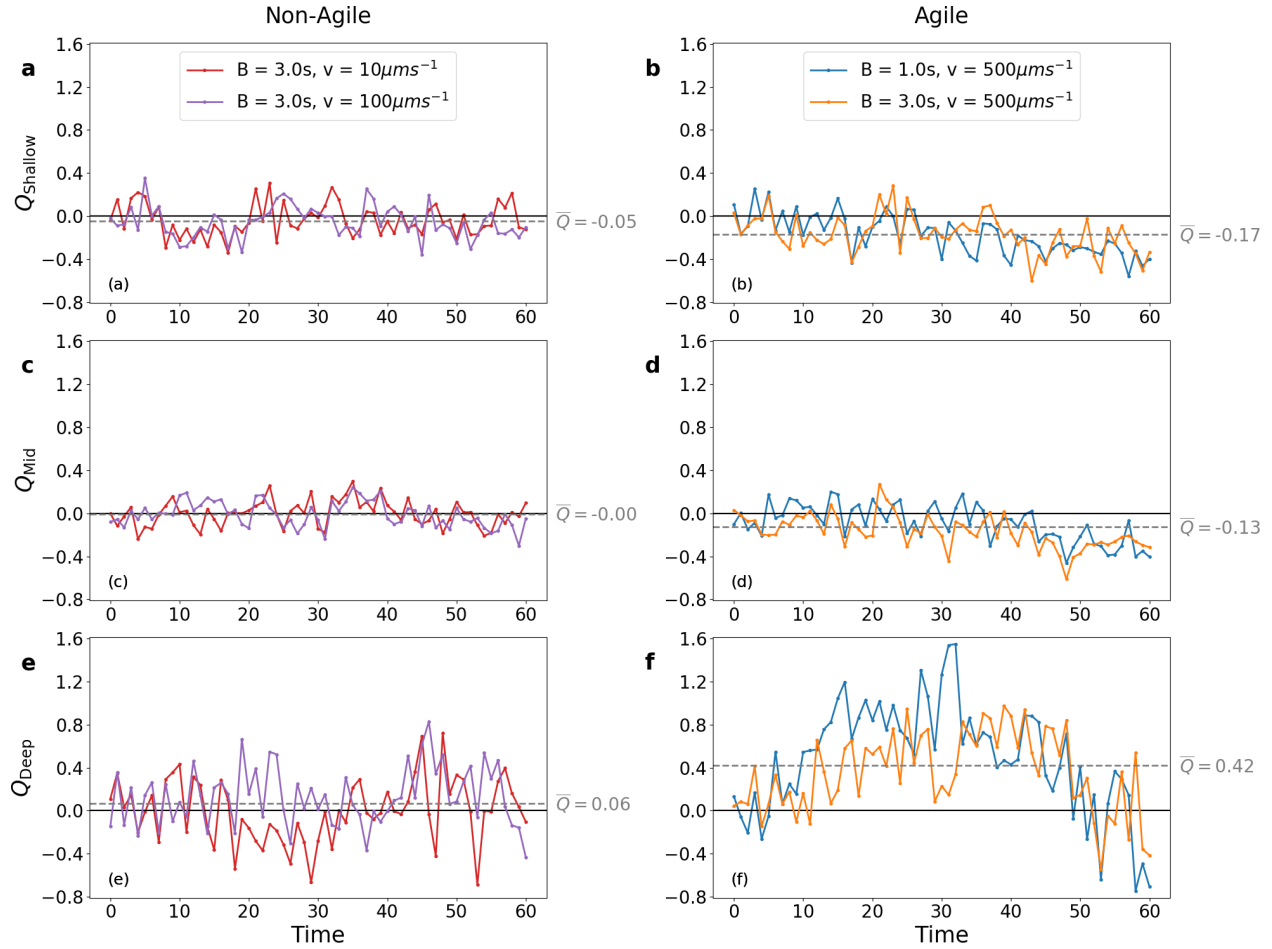


Figure 3: Q -statistic over time (solid lines) in different depth regions. Subplots in the left-hand column, (a), (c), (e), are from two simulated microbe populations representative of non-agile microbe behaviour. Subplots in the right-hand column, (b), (d), (f), are from two simulated microbe populations representative of agile microbe behaviour. Within each subplot, the dashed gray line represents the mean value \bar{Q} (w.r.t. time) of the Q -statistic for the two simulations and depth region plotted therein. Non-agile microbes are not more concentrated in patches than non-motile microbes, whereas agile microbes in the deep region exhibit modest patch enhancement. We note that agile microbes in the shallower regions exhibit weak but negative mean patch enhancement. Full results for every combination of motility parameters (B, v_{swim}) and each depth region are plotted in Supplementary Figs. 4–6.

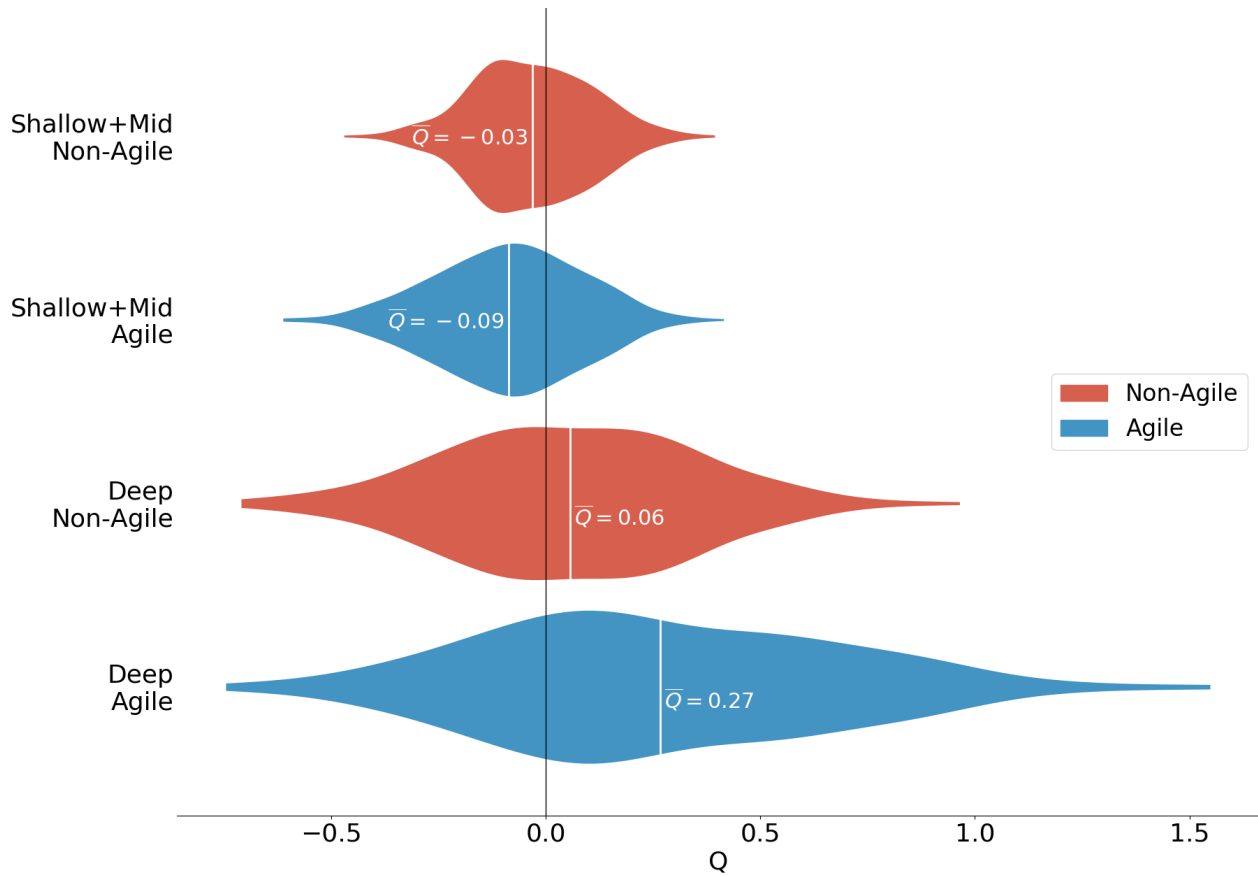


Figure 4: Violin plot comparison of the distribution of Q -values at all times for agile and non-agile microbes in the combined Shallow-Mid regions and the Deep region. Mean values are marked in white. Microbes in the Shallow-Mid regions exhibit weak negative mean patch enhancement, in contrast to positive mean patch enhancement in the Deep region. Furthermore, only in the Deep region are microbes able to attain strong patch enhancement ($Q \geq 1$).

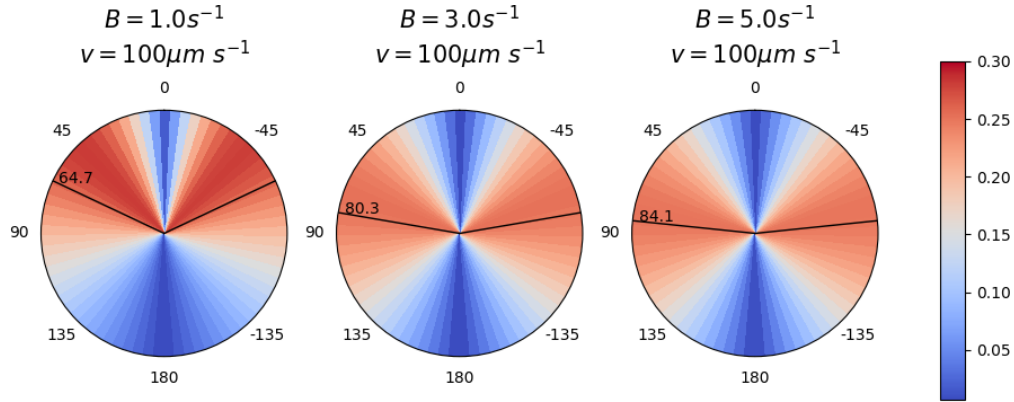


Figure 5: Normalised distributions of microbe polar angles between 20 – 60s in three motile simulations with $v_{\text{swim}} = 100 \mu\text{m s}^{-1}$ and $B = 1\text{s}^{-1}$, $B = 3\text{s}^{-1}$ and $B = 3\text{s}^{-1}$ respectively. A polar angle of 0° would represent orientation directly "upwards" towards the fluid surface. Mean polar angles for each simulation are marked and annotated in black. Microbes are subject to a constant balancing between their inherent tendency to orient towards the vertical (captured by the reorientation timescale parameter B) and the disorienting effect of turbulence. Faster reorientation (small B) results in a more vertical orientation than in the case of slower reorientation (large B). Distributions for all combinations of motility parameters are plotted in Supplementary Fig. 7.

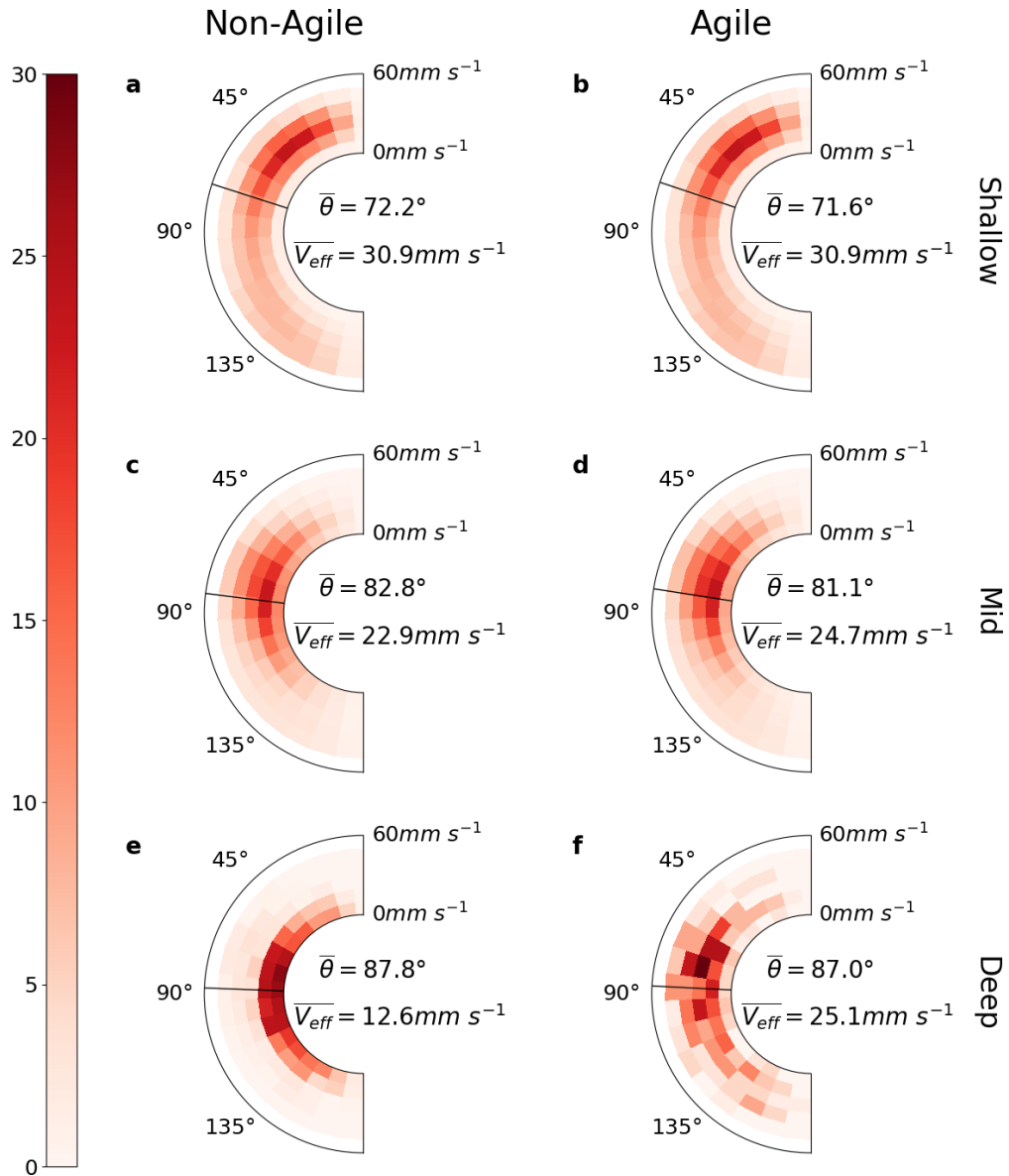


Figure 6: Normalised distributions of the magnitude and polar angle of effective velocity in each depth region of two simulations, respectively characteristic of non-agile (**a**, **c**, **e**) and agile (**b**, **d**, **f**) microbes. Microbes in the deep region have near-horizontal effective velocity, which acts to restrict their movement in the vertical direction. Also in the deep region, the difference in the magnitude of effective velocity (“effective speed”) is many times larger than the difference in microbial swimming speed. Elsewhere, effective speeds are very similar between all simulations, and the effective velocity is less vertically constrained.

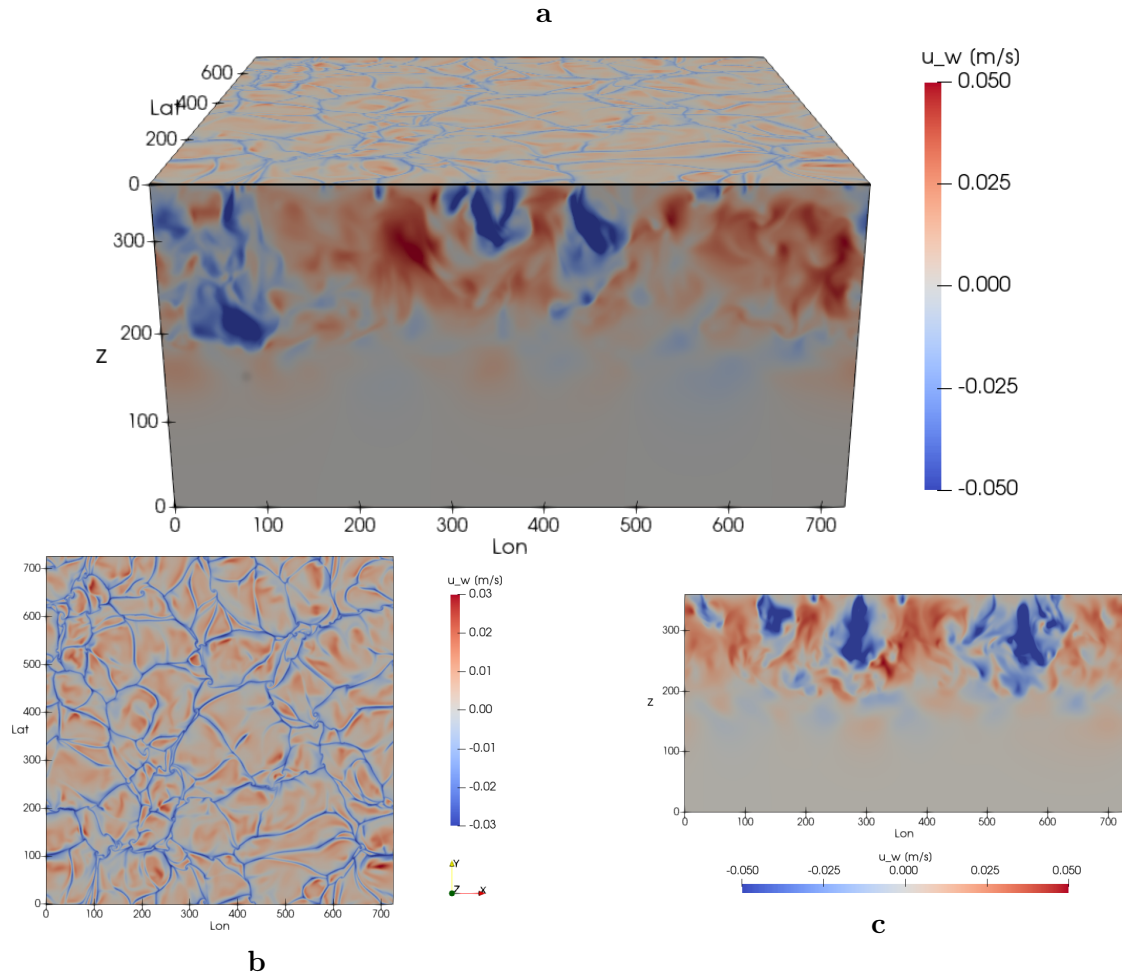


Figure 7: Vertical fluid velocities (in m s^{-1}) at $t = 60$ s during the SPARKLE DNS. Axes are labelled in units of DNS cell side-length. **(a)** shows the velocities at the surface and sides of the simulation. **(b)** is a top-down view of the fluid surface demonstrating rising regions of less dense fluid (red) pushing aside denser, falling fluid (blue). **(c)** is a side-on cross-section view through the center of the simulation, demonstrating the depth profile of these cooler (blue) and warmer (red) regions.